Journal of Sound and Vibration (2000) **234**(5), 859–880
doi:10.1006/jsvi.2000.2907, available online at http://www.idealibrary.com on IDEAL®

TRANSONIC AND LOW-SUPERSONIC AEROELASTIC ANALYSIS OF A TWO-DEGREE-OF-FREEDOM AIRFOIL WITH A FREEPLAY NON-LINEARITY

DONG-HYUN KIM AND IN LEE

Department of Aerospace Engineering, Korea Advanced Institute of Science and Technology, 373-1, *Kusong-Dong*, *Yusong-Gu*, *Taejon*, 305-701, *South Korea*

(*Received* 21 *July* 1999, *and in final form* 20 *January* 2000)

A two-degree-of-freedom airfoil with a freeplay non-linearity in the pitch and plunge directions has been analyzed in the transonic and low-supersonic flow region, where aerodynamic non-linearities also exist. The primary purpose of this study is to show aeroelastic characteristics due to freeplay structural non-linearity in the transonic and low-supersonic regions. The unsteady aerodynamic forces on the airfoil were evaluated using two-dimensional unsteady Euler code, and the resulting aeroelastic equations are numerically integrated to obtain the aeroelastic time responses of the airfoil motions and to investigate the dynamic instability. The present model has been considered as a simple aeroelastic model, which is equivalent to the folding fin of an advanced generic missile. From the results of the present study, characteristics of important vibration responses and aeroelastic instabilities can be observed in the transonic and supersonic regions, especially considering the effect of structural non-linearity in the pitch and plunge directions. The regions of limit-cycle oscillation are shown at much lower velocities, especially in the supersonic flow region, than the divergent flutter velocities of the linear structure model. It is also shown that even small freeplay angles can lead to severe dynamic instabilities and dangerous fatigue conditions for the flight vehicle wings and control fins.

1. INTRODUCTION

Structural non-linearities are subdivided into distributed non-linearities and concentrated ones. Distributed non-linearities are spread over the entire structure-like material and geometric non-linearity, but concentrated non-linearities have a local effect in a control mechanism or an attachment of external stores. Most flight vehicles may have inherently concentrated structural non-linearities such as freeplay, friction, hysteresis and preload in the hinge part of their control surfaces and folded sections, etc. Concentrated structural non-linearities may be generated from a worn or loose hinge connection of control surface, joint slippage, and manufacturing tolerance. Concentrated structural non-linearities are generally known to cause significant instabilities in the aeroelastic responses of aero-surfaces. Among all these several non-linearities, the freeplay usually gives the most critical flutter condition. The aeroelastic responses of the system with structural non-linearity have the four categories: damped stable motion, limit-cycle oscillation (LCO), chaotic motion and divergent flutter condition.

Flutter prevention technology in the transonic operating regime is an important problem in flight vehicle wing design and flight safety. Flutter is a dynamic instability phenomenon

0022-460X/00/300859 + 22 $35.00/0

resulting from interaction between an elastic structure and the flow around the structure. The large amplitudes and high frequencies associated with flutter phenomena can cause catastrophic structural failure. Flight vehicle wings that operate in transonic flow experience increased susceptibility to flutter. It has been widely reported that the flutter-onset speed gradually decreases with an increasing Mach number, reaching a minimum in the transonic regime, followed by an upward rise in the supersonic regime [1]. The minimum of this curve, or flutter boundary, is called the "flutter dip". Analysis of the flutter dip is primarily of significance to design engineers, since the transonic regime is typically within the flight envelope of these flight vehicles. In the transonic speeds, aerodynamic non-linearities become dominant due to the shock waves or the shock-induced separations on the airfoil surface.

A two-degree-of-freedom airfoil system (typical section model) can give a lot of insights and useful information about the physical aeroelastic phenomena. Many aeroelastic analyses and investigations for the linear typical section model in the transonic flow regime have been widely performed using the technique of computational fluid dynamics (CFD) since the mid-1970s [2–9]. However, most of the previous studies in the transonic region have the assumption of structural linearity. Recently, in the case of considering the structural non-linearity, many researchers have also conducted good work, although most of them are restricted to the subsonic regions [10–15]. Hence, this paper purports to observe the effects of aerodynamic non-linearity due to the strong shock motion in the transonic and low-supersonic flow regions. The main purpose of this article is to present structural non-linearity effects on aeroelastic responses in the flow region with aerodynamic non-linearity by using the simultaneous time-integration method coupled with CFD code of the Euler-based compressible aerodynamic theory. This paper also shows the combined non-linear effects of pitch-plunge freeplay for a typical section model. The combined

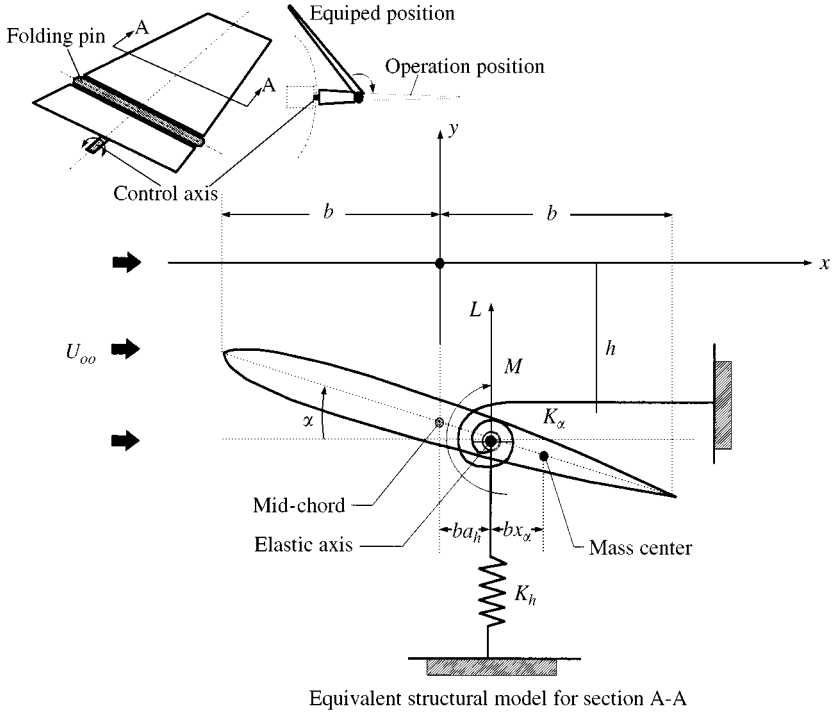

Figure 1. Typical section model.

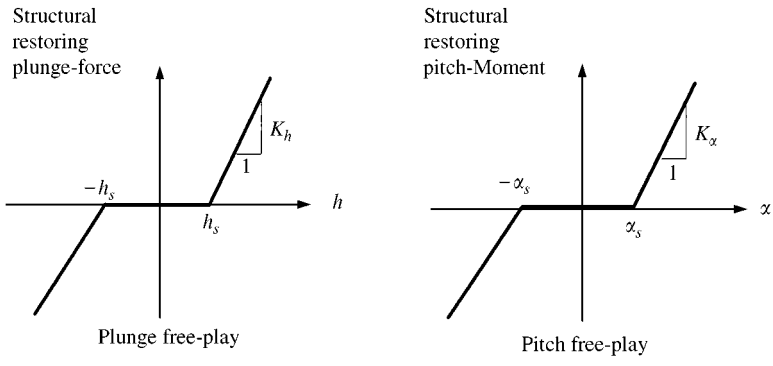

Figure 2. Non-linear plunge and pitch stiffness.

plunge-pitch freeplay can usually be seen in an advanced generic missile pin that could be folded at its settled position. Actually, a multi-purpose military missile fin with folded mechanism may have two-axial non-linearities at both the folding fin axis and pitch control axis, as shown in Figure 1. In this paper, an equivalent typical section model with two-degree-of-freedom motion and with freeplay non-linearity in both the plunge and pitch directions, as shown in Figure 2, has been considered. The unsteady aerodynamic forces on the airfoil were evaluated using the two-dimensional unsteady Euler code, and the resulting aeroelastic equations are integrated numerically to give the aeroelastic time responses of the airfoil motion and to show the dynamic instability. In this study, transonic limit-cycle behaviors and flutter boundaries of a two-degree-of-freedom aeroelastic system were calculated. The transonic and supersonic flutter analysis results in both the linear and non-linear cases are compared to show the pitch-plunge freeplay effects on the flutter boundary.

2. THEORETICAL ANALYSIS

2.1. NON-LINEAR AEROELASTIC MODEL

The aeroelastic model considered here is a two-degree-of-freedom system, free to rotate in the x–y plane and free to translate in the vertical direction as shown in Figure 1 which also shows the notation used for the analysis of the airfoil system oscillating in pitch and plunge. The plunging deflection is denoted by h, positive in the downward direction at the elastic axis (EA); α is the pitch angle about the elastic axis, positive in the nose-up rotation. The elastic axis is located at a distance ba from midchord, while the mass center is located at a distance $x_\alpha b$ from the elastic axis. Both distances are positive when measured toward the trailing edge of the airfoil. Note that the pitching axis may be offset from the center of the mass of the airfoil from the mid-chord, leading to a coupling between the pitching and plunging degree of freedom. The airfoil is assumed to be constrained to move along the vertical y-axis and to rotate about an elastic axis.

The well-known equations of motion for the typical section model in terms of the co-ordinates h and α can be derived from Lagrange's equation [16]. For non-linear restoring moment from springs with freeplay in the plunge and torsion degree of freedom (Figure 2), the governing aeroelastic equations of motion can be written as

$$m\ddot{h} + S_\alpha \ddot{\alpha} + g_h \dot{h} + F(h) = -L(t), \tag{1}$$

$$S_\alpha \ddot{h} + I_\alpha \ddot{\alpha} + g_\alpha \dot{\alpha} + G(\alpha) = M(t), \tag{2}$$

where the dot represents differentiation with respect to time; h is the airfoil vertical displacement at the elastic axis; I_α the airfoil moment of inertia (per unit span) about the pitch axis; m and S_α are the mass and static moment per unit span, and g_h and g_α are the structural damping coefficients for the pitching and plunging motions respectively. $F(h)$ and $G(\alpha)$ are the non-linear functions representing the restoring force and moment respectively, and L and M are the applied external unsteady aerodynamic lift and moment respectively. From Figure 2, $F(h)$ and $G(\alpha)$ can be written as

$$f(h) = \begin{cases} K_h(h - h_s), & h > h_s, \\ 0, & -h_s < h < h_s, \\ K_h(h + h_s), & h < h_s, \end{cases} \tag{3}$$

$$g(\alpha) = \begin{cases} K_\alpha(\alpha - \alpha_s), & \alpha > \alpha_s, \\ 0, & -\alpha_s < \alpha < \alpha_s, \\ K_\alpha(\alpha + \alpha_s), & \alpha < \alpha_s, \end{cases} \tag{4}$$

where K_h and K_α are the plunge and torsional spring constants for the linear part as shown in Figure 2 respectively, and h_s and α_s are the initial freeplay magnitudes of plunge and pitch motions respectively.

With the following definitions, $\xi = h/c$, $x_\alpha = S_\alpha/bm$, $\omega_h = (K_h/m)^{1/2}$, $\omega_\alpha = (K_\alpha/I_\alpha)^{1/2}$, $r_\alpha = (I_\alpha/mb^2)^{1/2}$, $\zeta_h = g_h/2(mK_h)^{1/2}$, $\zeta_\alpha = g_\alpha/2(I_\alpha K_\alpha)^{1/2}$ and $U^* = U_\infty/b\omega_\alpha$, aeroelastic governing equations (1) and (2) can be normalized in the following matrix form:

$$[M]\{u''(\tau)\} + [C]\{u'(\tau)\} + [K]\{u(\tau)\} = \{F_a(\tau)\} - \{F_s(u(\tau))\}, \tag{5}$$

where

$$[M] = \frac{1}{M_\infty^2}\begin{bmatrix} 1 & \dfrac{x_\alpha}{2} \\ \dfrac{2x_\alpha}{r_\alpha^2} & 1 \end{bmatrix}, \quad [C] = \frac{1}{M_\infty}\begin{bmatrix} 4\zeta_h\dfrac{\bar\omega}{U^*} & 0 \\ 0 & 4\zeta_\alpha\dfrac{1}{U^*} \end{bmatrix}, \quad [K] = \begin{bmatrix} f(\xi) & 0 \\ 0 & g(\alpha) \end{bmatrix}, \tag{6}$$

$$\{u(\tau)\} = \begin{Bmatrix} \xi(\tau) \\ \alpha(\tau) \end{Bmatrix}, \quad \{F_a(\tau)\} = \begin{Bmatrix} \dfrac{-2c_l(\tau)}{\pi\mu} \\ \dfrac{8c_m(\tau)}{\pi\mu r_\alpha^2} \end{Bmatrix}, \quad \{F_s(\tau)\} = \begin{Bmatrix} f_0(\xi) \\ g_0(\alpha) \end{Bmatrix}, \tag{7}$$

$$f(\xi) = \begin{cases} 4\left(\dfrac{\bar\omega}{U^*}\right)^2\xi(\tau), \\ 0 \\ 4\left(\dfrac{\bar\omega}{U^*}\right)^2\xi(\tau), \end{cases} \qquad f_0(\xi) = \begin{cases} -4\left(\dfrac{\bar\omega}{U^*}\right)^2\xi_s, & \xi(\tau) > \xi_s \\ 0 & -\xi_s \leqslant \xi(\tau) \leqslant \xi_s, \\ 4\left(\dfrac{\bar\omega}{U^*}\right)^2\xi_s, & \xi(\tau) < -\xi_s \end{cases} \tag{8}$$

$$g(\alpha) = \begin{cases} 4\left(\dfrac{1}{U^*}\right)^2\alpha(\tau) \\ 0 \\ 4\left(\dfrac{1}{U^*}\right)^2\alpha(\tau) \end{cases} \qquad g_0(\alpha) = \begin{cases} -4\left(\dfrac{1}{U^*}\right)^2\alpha_s, & \alpha(\tau) > \alpha_s \\ 0 & -\alpha_s \leqslant \alpha(\tau) \leqslant \alpha_s, \\ 4\left(\dfrac{1}{U^*}\right)^2\alpha_s, & \alpha(\tau) < -\alpha_s \end{cases} \tag{9}$$

In the above equations, the prime denotes differentiation with respect to the non-dimensional time $\tau(=\alpha_\infty t/c)$. Equation (5) can be written as a system of the first order ordinary differential equations. Let $\dot{\xi}(\tau)=\eta(\tau)$ and $\dot{\alpha}(\tau)=\beta(\tau)$. After substituting these equations into the structural equation (5), we can obtain the following equation of motion in the state-space matrix form:

$$\{\dot{y}(\tau)\}=\begin{bmatrix}[0] & [1]\\ -[M]^{-1}[K] & -[M]^{-1}[C]\end{bmatrix}\{y(\tau)\}+\begin{bmatrix}[0] & [0]\\ [0] & [M]^{-1}\end{bmatrix}\{Y(\tau)\}, \tag{10}$$

where

$$\{y(\tau)\}=\begin{Bmatrix}\dot{\xi}(\tau)\\ \dot{\alpha}(\tau)\\ \dot{\eta}(\tau)\\ \dot{\beta}(\tau)\end{Bmatrix}, \quad \{Y(\tau)\}=\begin{Bmatrix}0\\ 0\\ -\dfrac{2c_l}{\pi\mu}-f_0\\ \dfrac{8c_m}{\pi\mu r_\alpha^2}-g_0\end{Bmatrix}. \tag{11}$$

In the present study, a fifth order Runge–Kutta method is used to integrate numerically the non-linear equation (10) forward in time. Since the inverse matrix of $[M]$ can be determined analytically, an exact symbolic form of the inverse matrix of $[M]$ is applied.

2.2. NON-LINEAR AERODYNAMIC MODEL

The steady and unsteady flow quantities are obtained from the two-dimensional time-dependent Euler equations. For the unsteady aerodynamic or aeroelastic response analyses, an arbitrary Lagrangean–Eulerian (ALE) formulation for the Euler equations is used to calculated flow flux in the computational flow field with moving boundaries. The integral form of the two-dimensional Euler equations by ALE formulation can be written as

$$\frac{\mathrm{d}}{\mathrm{d}t}\int_{\Omega(t)} W\,\mathrm{d}A+\int_{\partial\Omega(t)}(F\,\mathrm{d}y-G\,\mathrm{d}x)=0, \tag{12}$$

where Ω is an element area with (moving) boundaries $\partial\Omega$ and the vector of conserved variable W and the convective fluxes F and G are given by

$$W=\begin{Bmatrix}\rho\\ \rho u\\ \rho v\\ \rho e\end{Bmatrix}, \quad F=\begin{Bmatrix}\rho(u-x_\tau)\\ \rho(u-x_\tau)u+p\\ \rho(u-x_\tau)v\\ \rho(u-x_\tau)e+up\end{Bmatrix}, \quad G=\begin{Bmatrix}\rho(v-y_\tau)\\ \rho(v-y_\tau)u\\ \rho(v-y_\tau)v+p\\ \rho(v-y_\tau)e+vp\end{Bmatrix}. \tag{13}$$

Here p, ρ, u, v and e are the pressure, the density, the Cartesian velocity components, and the specific total energy respectively. x_τ and y_τ are the Cartesian velocity components of the moving boundary $\partial\Omega$. For a calorically perfect gas, the pressure is related to the total energy by the equation of state

$$p=(\gamma-1)\left\{e-\rho\frac{u^2+v^2}{2}\right\}, \tag{14}$$

where γ is the ratio of specific heats.

In the present method, all the flow variables are normalized to keep the consistency for the aeroelastic equation (5) that is previously normalized by structural parameters. A finite-volume spatial discretization method is used on a structure grid to solve equation (1). The spatial derivatives are approximated by evaluating the net flux across the faces of each mesh cell using constant values of the velocities on each face. The dependent variables are defined at the cell centers. This approximation is equivalent to a central difference scheme that is second-order-accurate in the mesh spacing in the physical domain when the mesh is smooth. The central-difference spatial discretization requires the artificial dissipation to prevent numerical oscillations near the strong shock waves. In the present study, a directionally scaled dissipation model has been used explicitly. This dissipation model provides anisotropic dissipation to each direction, resulting in improved performance on meshes with high aspect ratio cells.

The diagonalized alternating direction implicit (DADI) algorithm of Pulliam and Chaussee [17] is used to obtain the time-integration solution. This integration method is based on the diagonal form of the implicit approximate-factorization algorithm and is known to be first-order-accurate in time and temporally non-conservative although being conservative in space. Hence, the subiteration algorithm [18, 19] is used to increase the time accuracy of the present unsteady calculations. For the farfield boundary conditions, a characteristic analysis based on Riemann invariants is used to determine the values of flow variables on the outer boundary of the grid. A normal momentum method is applied to extrapolate necessary pressure from adjacent cell centers to the airfoil surface boundary.

On the fluid–structure interface, both a traction boundary condition and a kinematic compatibility condition have to be satisfied. The traction boundary condition represents the fluid pressure acting on the structure. In the case of inviscid fluid flow like in the present study, the kinematic boundary condition provides for the compatibility of the normal velocity across the fluid–structure interface. The grid topology for the current study is an O-type grid. The grid size used for all runs, unless otherwise stated, consists of 129 points defining the airfoil surface, 33 points normal to the surface and the far outer boundary is located at 25 chord length. This grid system was efficiently selected from a comparison of numerical convergence tests for the various grid types. To regenerate the grid system for the newly calculated airfoil position, the dynamic meshing algorithm based on the linear spring network has been adopted from reference [20].

3. NUMERICAL RESULTS AND DISCUSSION

To verify the accuracy of the present Euler code, steady and unsteady aerodynamic analyses are performed for a NACA 0012 airfoil section. The steady flow result is obtained at the free-stream Mach number of 0·8 and zero angle of attack. The results of steady pressure distributions on the airfoil surface are shown in Figure 3. The present results show very good agreement with the experimental data given in reference [21]. About 400–500 time steps were required for converged steady-state solutions, when spatially varying time steps were used. Figure 4 shows the comparison of unsteady results when a NACA 0012 airfoil with the pitch axis located at the quarter-chord is under a rigid pitch motion. This case has been previously studied by Venkatakrishnan and Jameson [22]. The results of the present unsteady lift and moment coefficients agree well with those of a previous calculation. In this unsteady calculation, 500 time steps were used for a typical cycle of oscillation.

To validate the present flutter analysis technique, a well-known typical section model is selected. This case was chosen since it has been previously studied by Yang *et al.* [5]

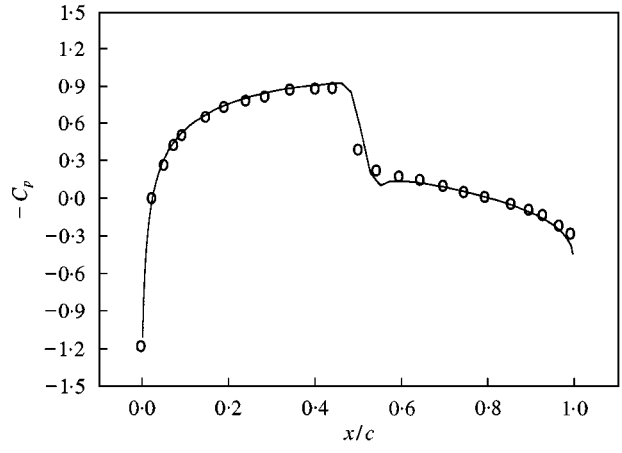

Figure 3. Steady pressure comparison for the NACA 0012 airfoil ($M = 0{\cdot}8$, $\alpha_0 = 0{\cdot}0^\circ$): ○, experiment [21]; ——, present Euler.

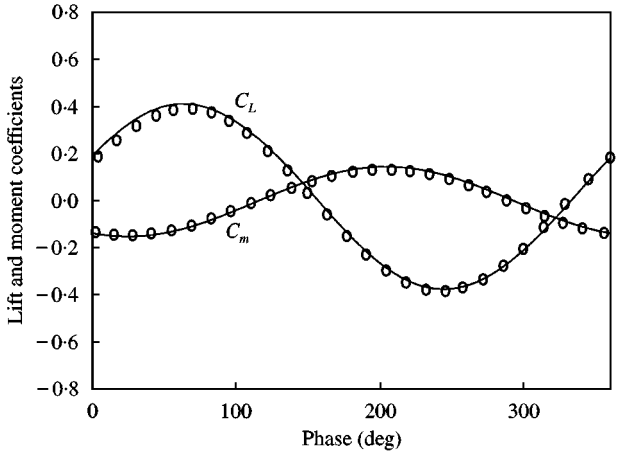

Figure 4. Unsteady lift and moment coefficients comparison during the fourth cycles of pitching oscillation ($M = 0{\cdot}8$, $\alpha_0 = 0{\cdot}0^\circ$, $\alpha_m = 5{\cdot}0^\circ$, $k = 1{\cdot}0$). ○, Euler [22]; ——, present Euler (129×33).

and also by Wu *et al.* [9]. Figure 5 shows the calculated flutter velocities for a two-degree-of-freedom aeroelastic model with a NACA 64A006 airfoil. However, no structural non-linearity such as freeplay was considered in this model. The related structural parameters given in Table 1 are selected to be the same values as the case presented in references [5, 9]. The airfoil–air mass ratio was varied to study the effect of airfoil to air mass ratio on the flutter characteristics. It was found that variations in airfoil to air mass ratio could lead to various dynamic characteristics such as damped oscillations, neutral oscillations or divergent (flutter) oscillations. The present results also show good agreements with previous analysis results by the UTRAN2 [5] and Euler [9] code.

To examine the effects of steady shock position on aeroelastic instability, steady pressure contours about NACA 0012 airfoil for four different Mach numbers are presented in Figure 6. The corresponding distributions of steady pressure coefficient at several Mach numbers are also presented in Figure 7. We can see that the pressure rises abruptly when the normal shock occurs on the mid-airfoil surface. It is noted here that there are severe changes

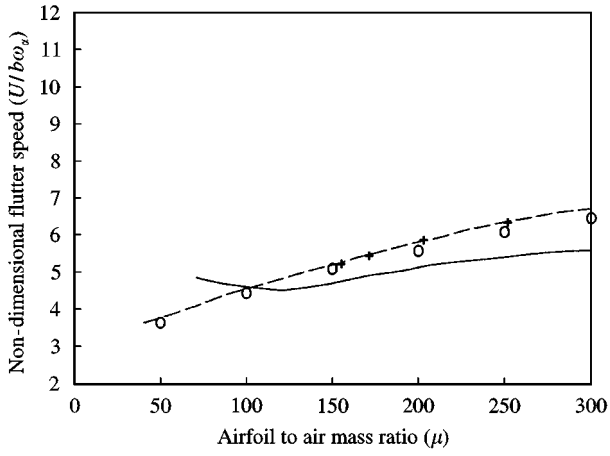

Figure 5. Flutter speed comparison for the various airfoil to air mass ratios (NACA 64A006 airfoil, $M = 0{\cdot}85$). – – –, UTRANS2; ——, LTRRN2; +, Euler [9]; ○, present Euler.

TABLE 1

Structural properties for typical section models

Model	Reference [9]	KL	KNA	KNH	KNAH
Airfoil section	64A006	0012	0012	0012	0012
a_h	− 0·5	− 0·25	− 0·25	− 0·25	− 0·25
x_α	0·25	0·25	0·25	0·25	0·25
r_α	0·5	0·629	0·629	0·629	0·629
$\bar{\omega}$	0·2	0·708	0·708	0·708	0·708
μ	50–300	36·15	36·15	36·15	36·15
α_s	•	•	0·001745	•	0·001745
h_s/c	•	•	•	0·001	0·001

in normal shock wave position on the airfoil surface between the Mach numbers of 0·8 and 0·9. These changes in shock positions are physically important to explain the transonic dip mechanism. In particular, the difference in pressure center on either the upper or lower surface due to the unsteady shock motion plays an important role in the large variation of pitching moment for the airfoil motion. This becomes the main reason for the increase in aeroelastic instability in the transonic flow regime.

Figures 8 and 9 show the examples of free vibration responses of the present aeroelastic system with or without structural non-linearity in its pitch and plunge degree of freedom. The related structural properties are given in Table 1. The freeplay non-linear model (KNA) presented in Table 1 is the same rigid model as studied in reference [15] and the only difference is the airfoil shape. The flat plate airfoil section was assumed in reference [15], but a NACA 0012 airfoil section has been selected in the present analysis. As can be expected, the free vibration responses have nothing to do with the airfoil shape in this case, because no aerodynamics is considered. For the linear structure model (KL) in Figure 8, the responses seem to be simple harmonic, but the phase diagram of the pitch-plunge freeplay non-linear model (KNAH) in Figure 9 shows banded multi-harmonic results for the same initial

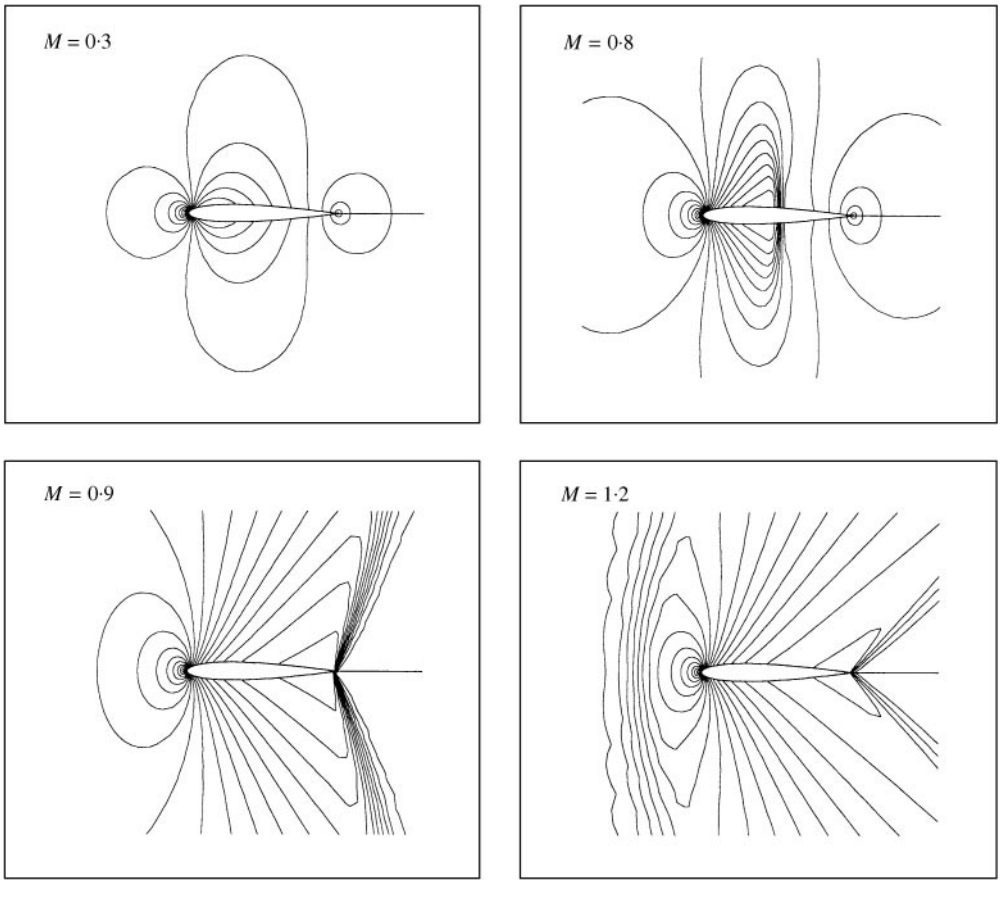

Figure 6. Steady pressure contours for the NACA 0012 airfoil.

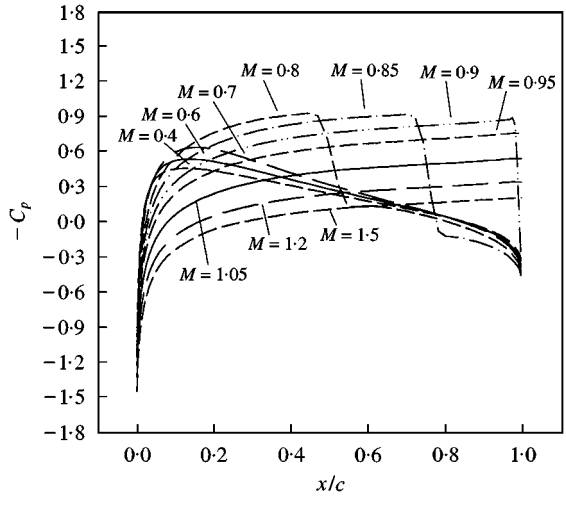

Figure 7. Steady pressure coefficients for the NACA 0012 airfoil.

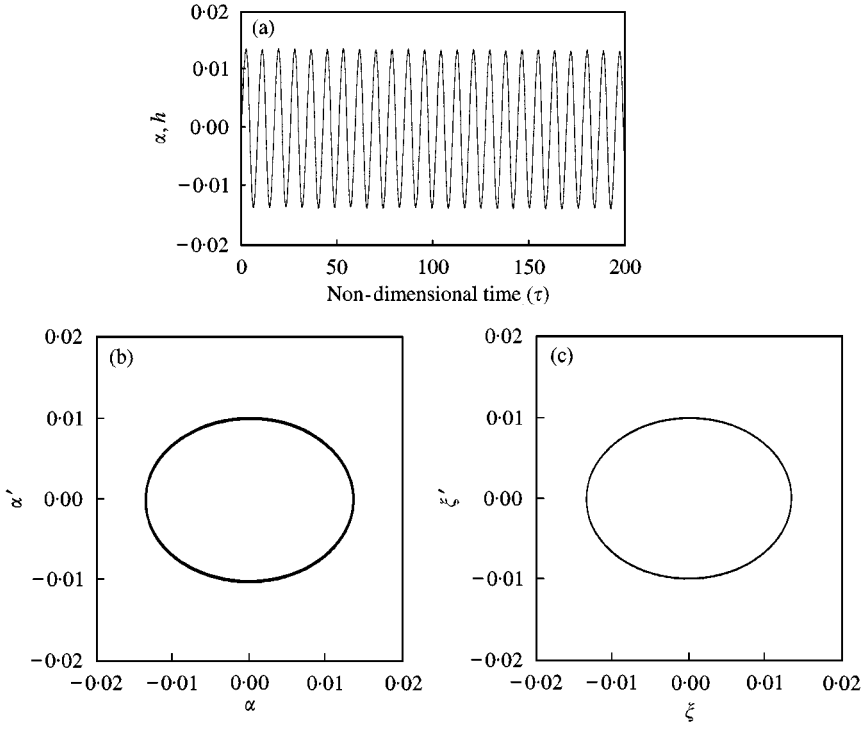

Figure 8. Free vibration time history and phase plane diagram for KL model ($U^* = 1{\cdot}8$, $\alpha'(0) = 0{\cdot}01$, $\xi'(0) = 0{\cdot}01$): (a) pitch and plunge response; ——, pitch; - - -, plunge; (b) pitch phase, (c) plunge phase.

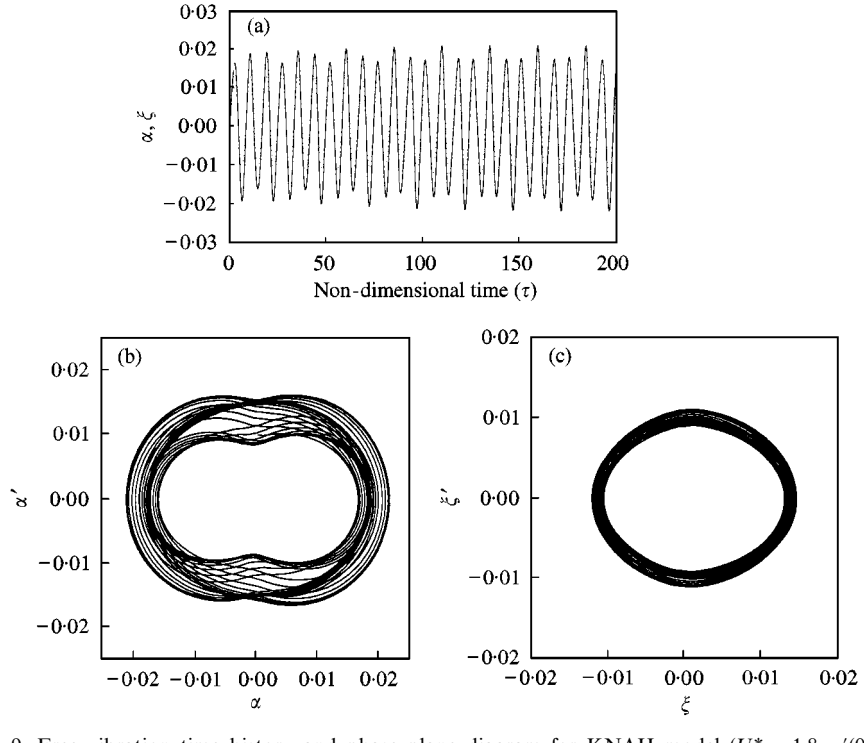

Figure 9. Free vibration time history and phase plane diagram for KNAH model ($U^* = 1{\cdot}8$, $\alpha'(0) = 0{\cdot}01$, $\xi'(0) = 0{\cdot}01$): (a) pitch and plunge response; ——, pitch; - - -, plunge; (b) pitch phase, (c) plunge phase.

conditions because of its non-linearity. But it is noted that the responses may vary greatly with the changes of initial conditions in this case. To consider the initial condition effects under the real flow condition, classical transonic flutter analyses were performed for the linear structure model. The flutter velocities and amplitudes of oscillation for the initial condition variation are presented in Table 2. We can see that the flutter velocity is slightly

TABLE 2

Calculated flutter velocity and magnitude of KL model for the various initial conditions at Mach 0·8

IC	A1	A2	A3	H1	H2	H3	AH1	AH2	AH3
$\bar{U}$	2·13	2·13	2·13	2·15	2·14	2·14	2·15	2·14	2·14
$\lvert\alpha\rvert$ (rad)	0·00028	0·0028	0·027	0·00022	0·0022	0·022	0·00022	0·0022	0·022
$\lvert h/c\rvert$	0.00036	0.0037	0.035	0.0003	0.003	0.029	0.0003	0.003	0.029

Note: [A1] $\alpha'(0) = 0{\cdot}001$, [A2] $\alpha'(0) = 0{\cdot}01$, [A3] $\alpha'(0) = 0{\cdot}1$; [H1] $\xi'(0) = 0{\cdot}0001$, [H2] $\xi'(0) = 0{\cdot}001$, [H3] $\xi'(0 = 0{\cdot}01$; [AH1] = [A1] + [H1], [AH2] = [A2] + [H2], [AH3] = [A3] + [H3].

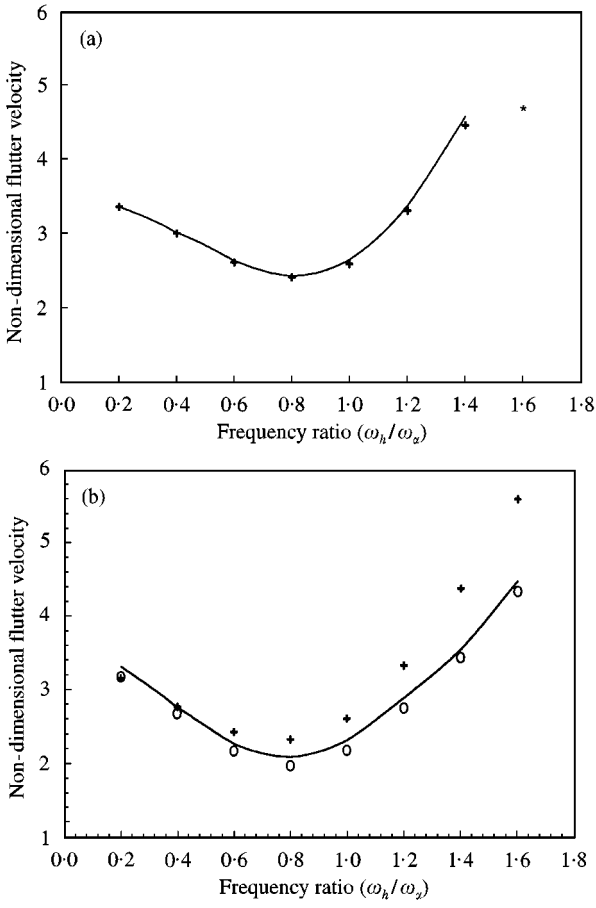

Figure 10. The effect of plunge to torsion frequency ratio on the flutter velocity: (a) $M = 0{\cdot}4$; (b) $M = 0{\cdot}8$; ——, present Euler; +, DLM; *, present Euler (divergence); ○, TSD2KR.

changed for the various initial conditions, but the amplitudes are varied linearly up to a certain velocity and converge for the larger initial disturbances. The types of dynamic responses at flutter condition, although not presented in this paper, are very similar to those of reference [9]. Actually, in the transonic flow region, the limit-cycle phenomenon usually shown in the responses of the non-linear structural model can also be observed in the linear structural model, since there are aerodynamic non-linearities due to the interactions of strong shock waves during the unsteady airfoil motion.

A comparison of flutter analysis results for the various natural frequency ratios is presented in Figure 10. The doublet lattice method (DLM) [15], the TSD2KR (two-dimensional version of reference [23]) and the present unsteady Euler codes were used for this comparison. In the vicinity of the frequency ratio of 1·0, it is shown that the flutter

TABLE 3

The parameter map of KNA model for the various initial velocities

	Dynamic response						
(a) $M = 0{\cdot}8$							
2·5	F	F	F	F	F	F	F
2·4	F	F	F	F	F	F	F
2·3	F	F	F	F	F	F	F
2·2	F	F	F	F	C	F	F
2·1	F	F	F	L	L	F	L
2·0	•	L	L	L	L	L	L
1·9	•	L	L	L	•	L	L
1·8	•	L	L	L	•	L	L
1·7	•	•	L	L	•	L	L
1·6	•	•	•	•	•	•	•
1·5	•	•	•	•	•	•	•
		[A1]	[A2]	[A3]	[H1]	[H2]	[H3]
	Linear	Non-linear (KNA model)					
(b) $M = 1{\cdot}2$							
3·6	F	F	F	F	F	F	F
3·5	F	L	L	L	L	L	L
3·4	•	L	L	L	L	L	L
3·3	•	L	L	L	L	L	L
3·2	•	L	L	L	L	L	L
3·0	•	L	L	L	L	L	L
2·8	•	L	L	L	L	L	L
2·6	•	L	L	L	L	L	L
2·4	•	L	L	L	L	L	L
2·3	•	L	L	L	L	L	L
2·2	•	L	L	L	L	L	L
2·1	•	L	L	L	L	L	L
2·0	•	•	L	L	L	L	L
1·9	•	•	L	L	•	L	L
1·8	•	•	•	•	•	•	•
		[A1]	[A2]	[A3]	[H1]	[H2]	[H3]
	Linear	Non-linear (KNA model)					

Note: F, divergent flutter; L, limit-cycle oscillation; C, Chaotic motion; •, convergent stable motion.

velocity tends to be minimal, as expected from classical aeroelastic phenomena. Since the doublet lattice technique was used in reference [15], the airfoil was assumed to be a flat plate in the previous results. The results of the different aerodynamic methods are very similar at Mach 0·4, as shown in Figure 10(a), because of the aerodynamic linearity in the subsonic flow region. But, it is noted that there are large differences in the flutter velocities at Mach 0·8. As mentioned before, there are strong shock wave interactions in the transonic flow regime, so that the linear aerodynamic theory like the doublet lattice technique cannot predict the correct flutter boundary. The reason for showing different flutter velocities at a high frequency ratio is that the weak torsion stiffness gives a large pitching amplitude, which causes a stronger shock motion. The results using the TSD code are very similar to those of the present Euler code since the TSD code can also consider the aerodynamic non-linearity.

The main purpose of this article is to investigate the structural non-linear effects on the aeroelastic responses in the transonic and low-supersonic flow regions, by using the simultaneous integration method directly coupled with CFD code of the Euler-based

TABLE 4

The parameter map of KNH model for the various initial velocities

$\bar{U}$	Dynamic response						
(a) $M = 0{\cdot}8$							
2·5	F	F	F	F	•	F	F
2·4	F	F	F	F	•	F	F
2·3	F	F	F	F	•	F	F
2·2	F	•	F	F	•	F	F
2·1	F	•	F	L	•	L	L
2·0	•	•	•	•	•	•	•
1·9	•	•	•	•	•	•	•
1·8	•	•	•	•	•	•	•
1·7	•	•	•	•	•	•	•
1·6	•	•	•	•	•	•	•
1·5	•	•	•	•	•	•	•
		[A1]	[A2]	[A3]	[H1]	[H2]	[H3]
	Linear	Non-linear (KNA model)					
(b) $M = 1{\cdot}2$							
3·6	F	•	F	F	•	F	F
3·5	F	•	L	L	•	L	L
3·4	•	•	L	L	•	L	L
3·3	•	•	L	L	•	L	L
3·2	•	•	L	L	•	L	L
3·1	•	•	L	L	•	L	L
3·0	•	•	•	•	•	L	L
2·9	•	•	•	•	•	•	L
2·8	•	•	•	•	•	•	•
2·6	•	•	•	•	•	•	•
2·5	•	•	•	•	•	•	•
2·4	•	•	•	•	•	•	•
		[A1]	[A2]	[A3]	[H1]	[H2]	[H3]
	Linear	Non-linear (KNH model)					

non-linear aerodynamic theory. As long as separation does not occur in the flow, the Euler equations provide a reasonable aerodynamic model for transonic flutter calculations, including the modelling of aerodynamic non-linearities that can result in limit-cycle behavior. In the present study, three types of freeplay non-linearities have been considered. The related structural properties of all models are given in Table 1. The time-domain analysis was carried out for the variation of initial disturbance and the reduced free-stream velocity. The results of the present analyses at Mach 0·8 and 1·2 are presented in the parameter map as shown in Tables 3 and 4. Detailed time responses are generally classified into four categories: damped stable motion, limit-cycle oscillation (LCO), chaotic motion and divergent flutter. The aeroelastic characteristics of the non-linear structural models tend to be less affected by the initial disturbed velocities like the cases of linear structure. The calculated divergent flutter speed is almost the same as that of the linear structure given in Table 2.

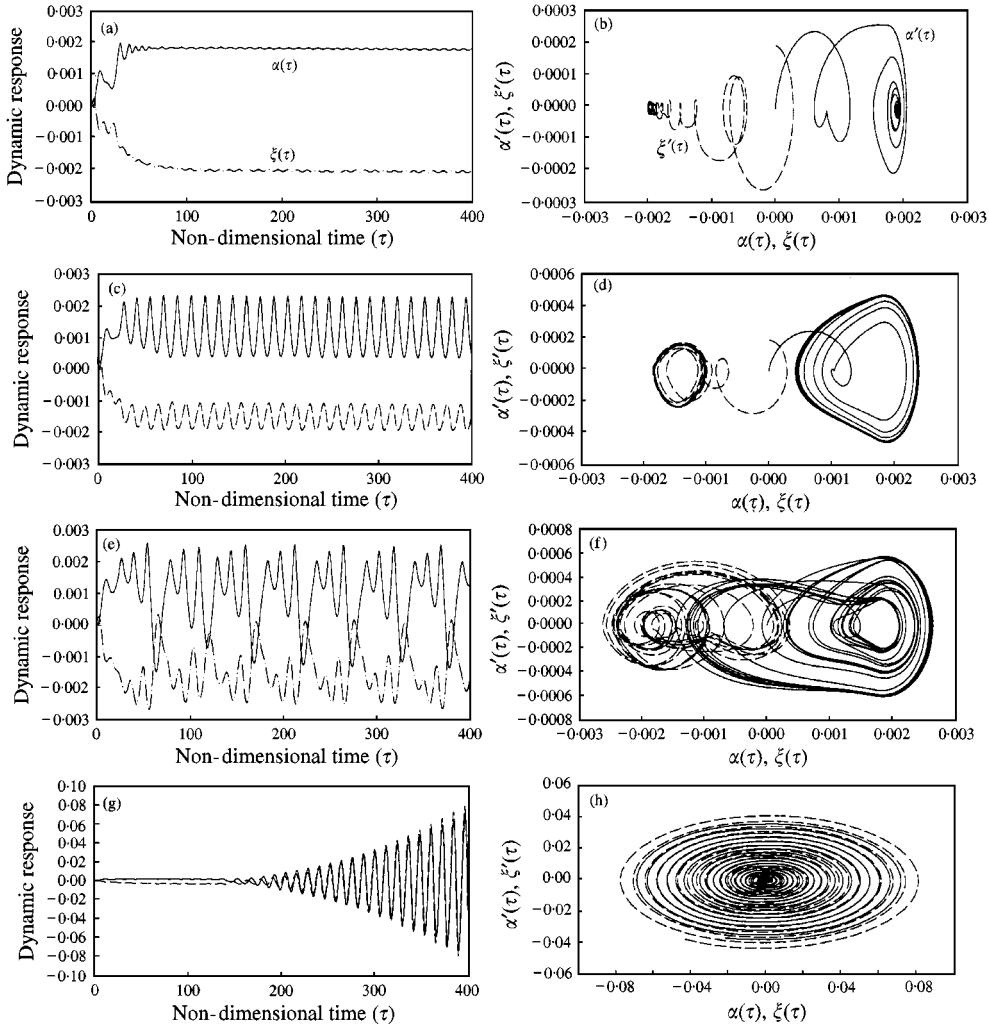

Figure 11. Non-linear aeroelastic responses for the KNA model ($M = 0{\cdot}8$, $\xi'(0) = 0{\cdot}0001$): (a), (b) $U^* = 1{\cdot}9$; (c), (d) $U^* = 2{\cdot}0$; (e), (f) $U^* = 2{\cdot}2$; (g), (h) $U^* = 2{\cdot}3$; ——, pitching motion; – – – plunging motion.

The examples of detailed time history and phase diagrams for the pitch and plunge motions at the elastic axis are shown in Figures 11–14. These responses include the limit-cycle oscillations and chaotic motions. Figures 11 and 12 are the aeroelastic responses of KNA model for the variation of reduced velocity with the two different initial conditions. In Figure 11, a converged response is obtained at $U^* = 1{\cdot}9$ and divergent flutter at $U^* = 2{\cdot}3$. But there are limit-cycle oscillations at $U^* = 2{\cdot}0$ and chaotic motion at $U^* = 2{\cdot}2$ because of the effect of combined aero-structural non-linearity. Chaotic motions as shown in Figures 11(e) and 11(f) cannot be seen in the usual transonic responses of a linear structure model. Figure 12 shows the responses for the different initial conditions of plunge direction ($\xi'(0) = 0{\cdot}001$) at the same Mach number. Unlike the previous results in Figure 11, it shows that the limit-cycle oscillations are dominant. These trends of different responses indicate the typical dependency of the initial condition for a non-linear system. For the

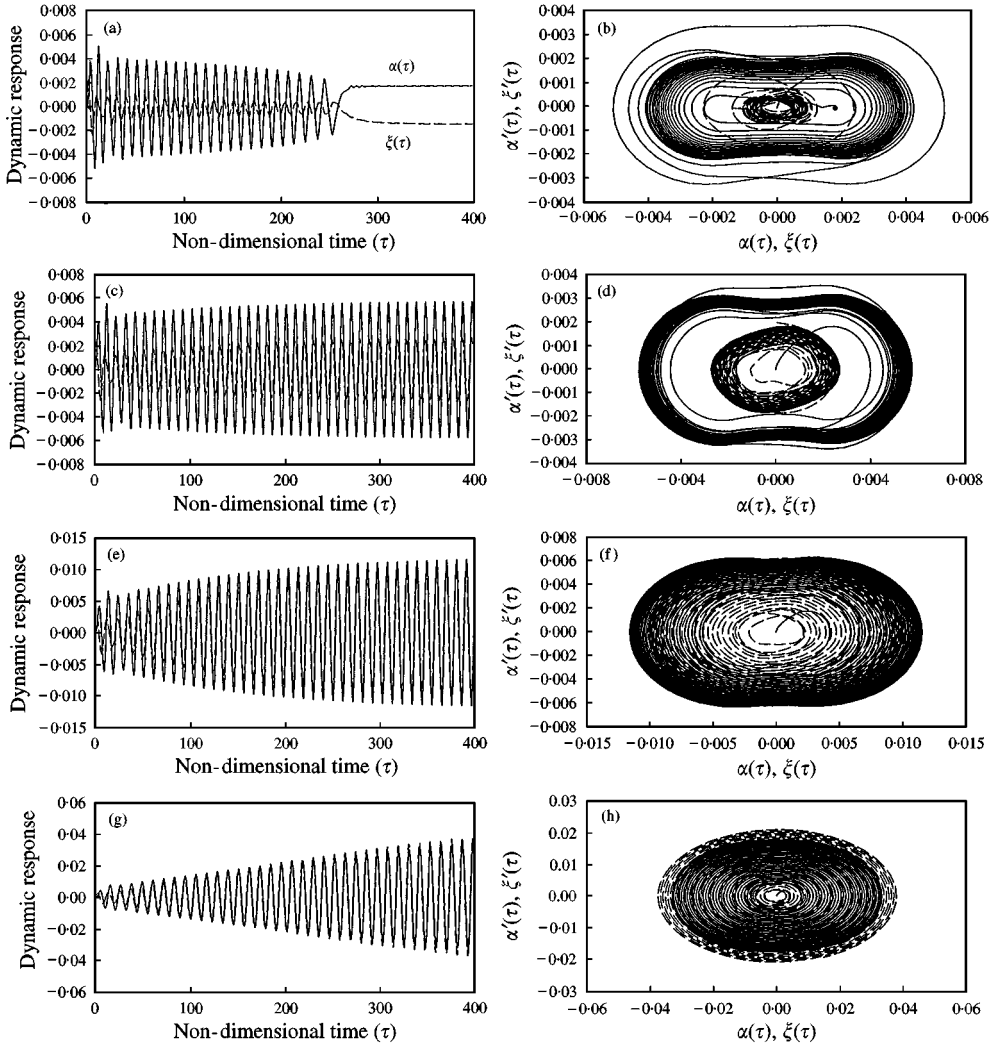

Figure 12. Non-linear aeroelastic responses for the KNA model ($M = 0{\cdot}8$, $\xi'(0) = 0{\cdot}001$): (a), (b) $U^* = 1{\cdot}6$; (c), (d) $U^* = 1{\cdot}7$; (e), (f) $U^* = 1{\cdot}9$; (g), (h) $U^* = 2{\cdot}1$; ——, pitching motion; – – – plunging motion.

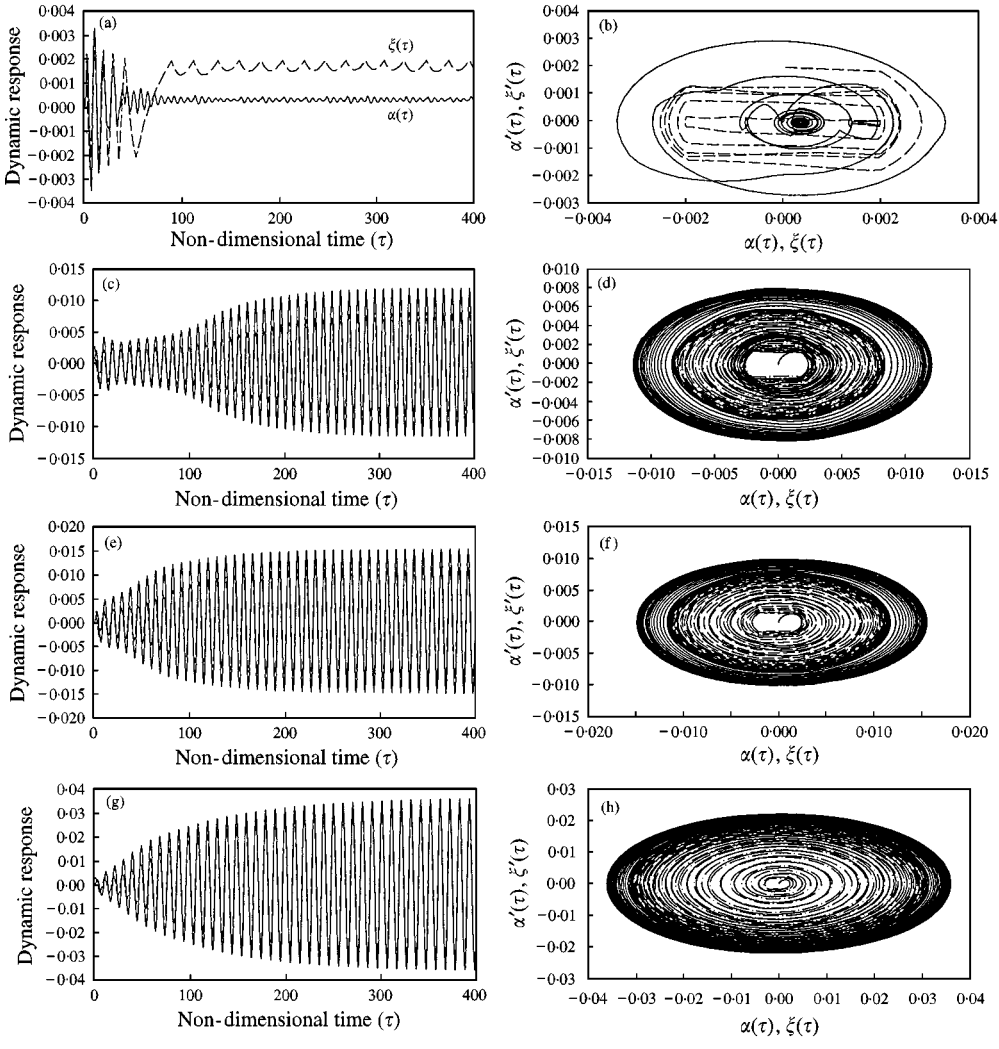

Figure 13. Non-linear aeroelastic responses for the KNH model ($M = 1{\cdot}2$, $\xi'(0) = 0{\cdot}0001$): (a), (b) $U^* = 2{\cdot}9$; (c), (d) $U^* = 3{\cdot}0$; (e), (f) $U^* = 3{\cdot}1$; (g), (h) $U^* = 3{\cdot}3$; ——, pitching motion; – – – plunging motion.

structural linear case with the same condition, there are only converged responses regardless of the initial conditions. Time-domain analyses were carried out for the various initial disturbances and free-stream velocities. The detailed results at Mach numbers of 0·8 and 1·2 are represented in the parameter map as shown in Table 3. Time responses are classified into four categories: damped stable motion (●), limit-cycle oscillation (L), chaotic motion (C) and divergent flutter (F).

Four sampled responses of the KNH model at Mach 1·2 are given in Figure 13. We can also see the converged response at low velocity and the limit-cycle oscillations under the flutter velocity of the linear structure model. Chaotic motions have not been observed in this case. Although freeplay non-linearity exists in the plunge direction, it is shown that the pitch amplitude of limit cycle oscillation is larger than the plunge amplitude. Time-domain analyses were carried out for the various initial disturbances and free-stream velocities. The detailed results at Mach 0·8 and 1·2 are also represented in the parameter map as shown in

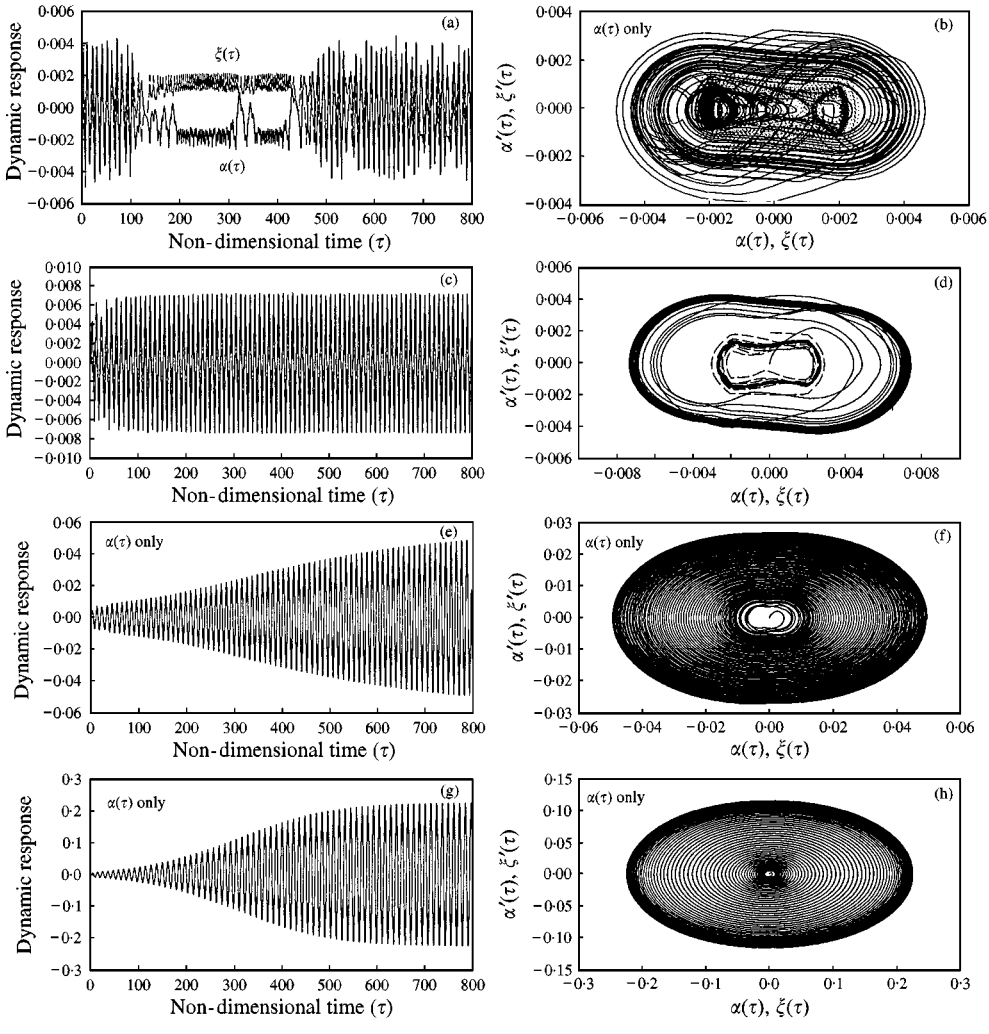

Figure 14. Non-linear aeroelastic responses for the KNAH model ($M = 0{\cdot}8$, $\xi'(0) = 0{\cdot}0001$): (a), (b) $U^* = 1{\cdot}5$; (c), (d) $U^* = 1{\cdot}7$; (e), (f) $U^* = 2{\cdot}1$; (g), (h) $U^* = 2{\cdot}3$; ——, pitching motion; – – – plunging motion.

Table 4. For the combined freeplay case of the KNAH model, four sampled responses are presented in Figure 14. The complex chaotic motions are shown at $U^* = 1{\cdot}5$, but it is noted that the magnitudes of these unstable chaotic responses are very small. Therefore, these results indicate that those vibration effects will not be severe for the aspect of structural dynamic instability.

Figure 15 shows the flutter boundary comparison between linear and non-linear structure models. A lot of computation work has been conducted to obtain the results, and corresponding parametric maps were constructed to find the minimum velocities, such as Tables 3 and 4. In these figures, the solid line indicates the flutter boundary of the linear model (KL) which has no freeplay in any direction. Figure 15(a) shows the flutter boundary of the KNA model with a freeplay in the pitch direction only. It is very important that there is a wide range of LCO region under the flutter boundary of the linear structural model. Therefore, in the above case, a structure can easily become dynamically unstable and constitute very dangerous conditions for fatigue failure. From this physical aspect, it can be

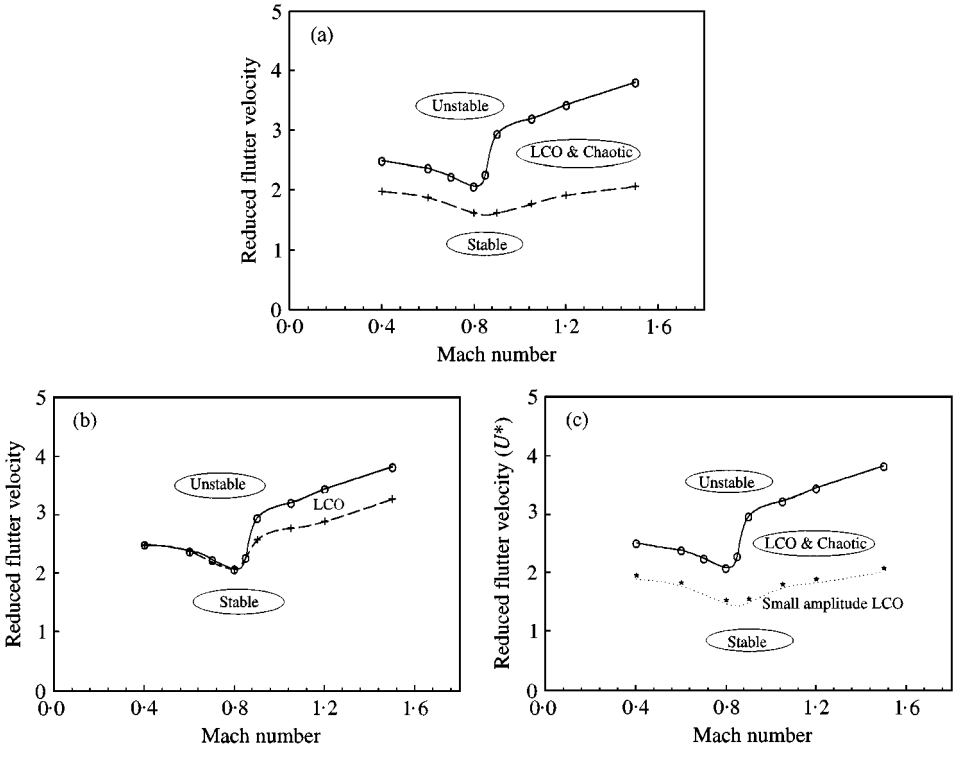

Figure 15. Flutter boundary comparison between linear and non-linear structural models: (a) pitch freeplay model, $\alpha_s = 0{\cdot}1^\circ$; (b) plunge freeplay model ($\xi_s = 0{\cdot}001$); (c) pitch-plunge freeplay model ($\alpha_s = 0{\cdot}1^\circ$, $\xi_s = 0{\cdot}001$); ○, divergent flutter boundary; + , minimum LCO boundary, *, small-amplitude LCO boundary.

suggested that if the freeplay exists in one direction, the apparent stiffness of the system tends to become weak in that direction as the initial freeplay angle is increased. This seems to be the main reason for the existence of limit-cycle oscillations and chaotic behaviors at much lower velocities and these trends can also be observed in Table 5. Figure 15(b) shows the result of the KNH model with freeplay in the plunge direction only. The calculated flutter boundary is nearly the same as that of the linear structure, in this case, under about Mach 0·9. However, there is also a small LCO region from Mach 0·9 to 1·5. The existence of this LCO region can be explained as follows: since the dynamic pressures are lower in the sub-transonic region than in the super-transonic region, the weakness effect of equivalent plunge stiffness seems not be dominant because there is not enough amplitude of oscillation to constitute the global dynamic instability. But, in the high-velocity region, the plunge oscillation magnitude and velocity can be increased as amounts of increased dynamic pressure. This causes the increases of relative angle of attack as well. Thus, in this condition, the structure may obtain enough kinetic energy to generate and to keep the self-excited oscillation. The examples of detailed responses of the KNH model are presented in Figure 12 at Mach 1·2. From the results, we can see that the freeplay effect on the LCO becomes large in the high-speed region as shown in Figures 15(a) and 15(b). The pitch freeplay shows a more dominant influence on aeroelastic instability than the plunge freeplay. Finally, Figure 15(c) shows the result of the KNAH model with the freeplay in both the pitch and the plunge directions. We can also see the wide range of LCO and chaotic region under the calculated flutter boundary of the linear structure model. The type of minimum LCO

TABLE 5

The parameter map of KNA model for the various initial velocities and pitch freeplay angles

$\bar{U}$	Dynamic response ($M = 0{\cdot}8$)						
(a) $\alpha_s = 0{\cdot}1'$							
2·5	F	F	F	F	F	F	F
2·4	F	F	F	F	F	F	F
2·3	F	F	F	F	F	F	F
2·2	F	F	F	F	F	F	F
2·1	F	F	F	F	F	F	F
2·0	•	L (0·018)	L(0·018)	L(0·018)	L(0·020)	L(0·020)	L(0·020)
1·9	•	L(0·012)	L(0·012)	L(0·012)	L(0·012)	L(0·012)	L(0·012)
1·8	•	L(0·008)	L(0·008)	L(0·008)	L(0·008)	L(0·008)	L(0·008)
1·7	•	•	•	L(0·006)	L(0·006)	L(0·006)	L(0·006)
1·6	•	•	•	•	•	•	•
1·5	•	•	•	•	•	•	•
		0·001	0·005	0·01	0·001	0·005	0·01
		$\alpha'(0)$			$\xi'(0)$		
	Linear	Non-linear (KNA model)					
(b) $\alpha_s = 0{\cdot}5^\circ$							
2·5	F	F	F	F	F	F	F
2·4	F	F	F	F	F	F	F
2·3	F	F	F	F	F	F	F
2·2	F	L(0·006)	L(0·200)	L(0·200)	L(0·200)	L(0·200)	L(0·200)
2·1	F	L(0·005)	L(0·130)	L(0·130)	L(0·001)	L(0·130)	L(0·130)
2·0	•	•	L(0·080)	L(0·080)	•	L(0·080)	L(0·080)
1·9	•	•	L(0·054)	L(0·054)	•	L(0·054)	L(0·054)
1·8	•	•	L(0·040)	L(0·040)	•	L(0·040)	L(0·040)
1·7	•	•	•	L(0·028)	•	L(0·028)	L(0·028)
1·6	•	•	•	•	•	•	•
1·5	•	•	•	•	•	•	•
		0·001	0·005	0·01	0·001	0·005	0·01
		$\alpha'(0)$			$\xi'(0)$		
	Linear	Non-linear (KNA model)					
(c) $\alpha_s = 1.0^\circ$							
2·5	F	F	F	F	F	F	F
2·4	F	C(0·016)	F	F	C(0·016)	F	F
2·3	F	L(0·012)	F	F	C(0·016)	F	F
2·2	F	L(0·010)	L(0·25)	L(0·25)	L(0·010)	L(0·25)	L(0·25)
2·1	F	L(0·008)	L(0·19)	L(0·19)	L(0·008)	L(0·19)	L(0·19)
2·0	•	L(0·006)	L(0·14)	L(0·14)	L(0·006)	L(0·14)	L(0·14)
1·9	•	•	•	L(0·10)	•	L(0·10)	L(0·10)
1·8	•	•	•	L(0·07)	•	L(0·07)	L(0·07)
1·7	•	•	•	•	•	•	L(0·05)
1·6	•	•	•	•	•	•	•
1·5	•	•	•	•	•	•	•
		0·001	0·005	0·01	0·001	0·005	0·01
		$\alpha'(0)$			$\xi'(0)$		
	Linear	Non-linear (KNA model)					

Note: ( ), oscillation pitch amplitude, rad.

boundary presented by a dotted line is very similar to that of the pitch freeplay case as shown in Figure 15(a). From these results, we can also conclude that the pitch freeplay produces dominant dynamic instability and there are no more critical instabilities due to the co-existence of the pitch and the plunge freeplay.

4. CONCLUSIONS

Transonic and low-supersonic flutter analyses of a two-degree-of-freedom system with freeplay non-linearities have been studied. The analytical model discussed in this paper is based on the simplified equivalent model of an actual folding fin of a generic missile. Unsteady aerodynamic forces on the airfoil were evaluated using the two-dimensional unsteady Euler code and the resulting aeroelastic equations are numerically integrated to obtain the detailed aeroelastic time responses of the airfoil motion. From the results of the present study, characteristics of several vibration responses and aeroelastic instabilities can be observed in the transonic and low-supersonic regions considering the effect of freeplay non-linearity in the pitch and the plunge directions. The results for both structurally linear and non-linear cases are compared to show the effects on flutter boundary. The detailed aeroelastic responses of limit-cycle oscillations are also presented to show the vibration characteristics. The regions of limit-cycle oscillation are shown more at the much lower velocities, especially in the supersonic flow region, than the divergent flutter velocities of the linear structure model. It is also shown that even small freeplay angles can lead to severe dynamic instabilities and dangerous fatigue conditions for the flight vehicle wings or control fins. The initial condition effects on the amplitudes of limit-cycle oscillation are also investigated at several Mach numbers for the various reduced velocities. The present study contributes to a better understanding of the important effects of structural non-linearity in the transonic and low-supersonic flow regimes.

REFERENCES

1. J. W. Edwards and J. L. Thomas 1987 *AIAA* 87-0107. Computational methods for unsteady transonic flows.
2. W. F. Ballhaus and P. M. Goorjian 1977 *AIAA Journal* **15**, 1728–1735. Implicit finite difference computations of unsteady transonic flows about airfoils.
3. K. Isogai 1979 *AIAA Journal* **17**, 793–795. On the transonic-dip mechanism of flutter of a sweptback wing.
4. T. Y. Yang and J. T. Batina 1982 *AIAA* 82-0688. Transonic time-response analysis of three degree of freedom conventional and supercritical airfoils.
5. T. Y. Yang, P. M. Guruswamy and A. G. Stritz 1982 *Journal of Aircraft* **19**, 211–220. Application of transonic codes to flutter analysis of conventional and supercritical airfoils.
6. T. Y. Yang and C. H. Chen 1982 *Journal of Aircraft* **19**, 875–888. Transonic flutter and response analyses of two-degree of freedom airfoils.
7. J. W. Edward, R. M. Bennett, W. Whitlow Jr and D. A. Seidel 1983 *Journal of Aircraft* **20**, 899–906. Time-marching transonic flutter solutions including angle-of-attack effects.
8. S. R. Bland and J. W. Edward 1984 *Journal of Aircraft* **21**, 209–217. Airfoil shapes and thickness effects on transonic airloads and flutter.
9. J. C. Wu, K. R. V. Kaza and L. N. Sankar 1989 *Journal of Aircraft* **26**, 168–177. Technique for the prediction of airfoil flutter characteristics in separated flow.
10. R. D. Raush, J. T. Batina and H. T. Y. Yang 1990 *Journal of Aircraft* **27**, 436–443. Euler flutter analysis of airloads using unstructured dynamic meshes.
11. Z. C. Yang and L. C. Zhao 1988 *Journal of Sound and Vibration* **123**, 1–13. Analysis of limit cycle flutter of an airfoil in incompressible flow.

12. Z. C. YANG and L. C. ZHAO 1990 *Journal of Sound and Vibration* **138**, 245–254. Chaotic motions of an airfoil with non-linear stiffness in incompressible flow.
13. J.-K. LIU and L. C. ZHAO 1992 *Journal of Sound and Vibration* **154**, 117–124. Bifurcation analysis of airfoils in incompressible flow.
14. D. M. TANG and E. H. DOWELL 1983 *Journal of Sound and Vibration* **165**, 251–276. Comparison of theory and experiment for non-linear flutter and stall response of a helicopter blade.
15. S.-H. KIM and I. LEE 1996 *Journal of Sound and Vibration* **193**, 823–846. Aeroelastic analysis of a flexible airfoil with a freeplay non-linearity.
16. E. H. DOWELL 1995 *A Modern Course in Aeroelasticity*. Dordrecht: Kluwer Academic Publishers, third revised and enlarged edition. ISBN 0-7923-2788-8.
17. T. H. PULLIAM and D. S. CHAUSSEE 1981 *Journal of Computational Physics* **39**, 347–363. A diagonal form of an implicit approximate-factorization algorithm.
18. K. MASTUNO 1989 *AIAA Paper* 89-1992-CP. A time accurate iterative scheme for solving the unsteady compressible equations.
19. K. MASTUNO 1990 *NAL TR*-1006. δ^2-correction scheme for unsteady compressible Navier–Stokes equations.
20. B. A. ROBINSON, J. T. BATINA and H. T. Y. YANG 1990 *AIAA*-90-1032-CP. Aeroelastic analysis of wings using the Euler equations with a deforming mesh.
21. J. B. MCDEVITT and A. F. OKUNO 1985 *NASA TP*-2485. Static and dynamic procedure measurements on a NACA 0012 airfoil in the Ames High Reynolds Number Facility.
22. V. VENKATAKRISHANAN and A. JAMESON 1988 *AIAA Journal* **26**, 974–981. Computation of unsteady transonic flows by the solution of Euler equations.
23. D.-H. KIM, S. G. JI, I. LEE and J. H. KWON 1998 *Journal of the Korean Society for Aeronautical and Space Sciences* **26**, 1–9. Transonic aerodynamic analysis using transonic small disturbance equation.

APPENDIX A: LIST OF SYMBOLS

a	speed of sound
a_h	non-dimensional distance between mid-chord and section elastic axis
b	airfoil semi-chord
c	airfoil chord ($=2b$)
c_l	lift coefficient per unit span
c_m	moment coefficient per unit span
h	plunge displacement at the elastic axis, positive down
I_α	cross-section mass moment of inertia about its elastic axis, per unit span ($=\int_c x^2 \rho_s \mathrm{d}x$)
k	reduced frequency ($=\omega c/U_\infty$)
K_h	spring stiffness in plunge direction
K_α	spring stiffness in pitch direction
m	airfoil mass per unit span
M	Mach number
r_α	non-dimensional radius of gyration about elastic axis (EA)
S_α	static moment per unit span ($=mx_{cg}=\int_c x\rho_s \mathrm{d}x$)
t	physical time
x_α	non-dimensional static imbalance of the airfoil about its elastic axis; CG-EA offset
u, v	velocities in the x, y directions
U^*	reduced velocity ($=U_\infty/b\omega$)
U	free-stream velocity
α	angle of attack; also torsion deflection
μ	airfoil-to-air mass ratio ($=m/\pi\rho b^2$)
ξ	non-dimensional plunge displacement at elastic axis ($=h/c$)
ρ	air density
ρ_s	airfoil structural density
ω	circular frequency, rad/s
ω_α	uncoupled frequency in torsion
ω_h	uncoupled frequency in bending
$\bar{\omega}$	non-dimensional frequency ratio ($=\omega_h/\omega_\alpha$)
τ	non-dimensional time ($=ta_\infty/c$)

Subscripts

0	initial condition
∞	condition at upstream infinity

Superscripts

$( )'$	$= \mathrm{d}( )/\mathrm{d}\tau$, differentiation with respect to the non-dimensional time τ